

1-26-2022

Resonant Alfvén Waves in the Lower Auroral Ionosphere: Evidence for the Nonlinear Evolution of the Ionospheric Feedback Instability

Hassanali Akbari

NASA Goddard Space Flight Center, hassanali.akbari@nasa.gov

Anatoly Streltsov

Embry-Riddle Aeronautical University, streltsa@erau.edu

Robert Pfaff

NASA Goddard Space Flight Center

James Clemmons

University of New Hampshire, Durham

Henry Freudenreich

NASA Goddard Space Flight Center

See next page for additional authors

Follow this and additional works at: <https://commons.erau.edu/publication>



Part of the [Atmospheric Sciences Commons](#)

Scholarly Commons Citation

Akbari, H., Pfaff, R., Clemmons, J., Freudenreich, H., Rowland, D., & Streltsov, A. (2022). Resonant Alfvén waves in the lower auroral ionosphere: Evidence for the nonlinear evolution of the ionospheric feedback instability. *Journal of Geophysical Research: Space Physics*, 127, e2021JA029854. <https://doi.org/10.1029/2021JA029854>

This Article is brought to you for free and open access by Scholarly Commons. It has been accepted for inclusion in Publications by an authorized administrator of Scholarly Commons. For more information, please contact commons@erau.edu.

Authors

Hassanali Akbari, Anatoly Streltsov, Robert Pfaff, James Clemmons, Henry Freudenreich, and Douglas Rowland

JGR Space Physics

RESEARCH ARTICLE

10.1029/2021JA029854

Key Points:

- Localized large-amplitude Alfvén wave structures are observed simultaneously at two altitudes in dual-sounding rocket experiment
- Observations are interpreted as standing Alfvén waves “trapped” in the ionosphere and subjected to the ionospheric feedback instability
- Observations reveal signatures of nonlinear wave steepening in correlation with large variations of the background plasma density

Correspondence to:

H. Akbari,
hassanali.akbari@nasa.gov

Citation:

Akbari, H., Pfaff, R., Clemmons, J., Freudenreich, H., Rowland, D., & Streltsov, A. (2022). Resonant Alfvén waves in the lower auroral ionosphere: Evidence for the nonlinear evolution of the ionospheric feedback instability. *Journal of Geophysical Research: Space Physics*, 127, e2021JA029854. <https://doi.org/10.1029/2021JA029854>

Received 9 AUG 2021
Accepted 6 JAN 2022

Resonant Alfvén Waves in the Lower Auroral Ionosphere: Evidence for the Nonlinear Evolution of the Ionospheric Feedback Instability

Hassanali Akbari¹ , Robert Pfaff¹ , James Clemmons² , Henry Freudenreich¹, Douglas Rowland¹, and Anatoly Streltsov³ 

¹NASA Goddard Space Flight Center, Greenbelt, MD, USA, ²University of New Hampshire, Durham, NH, USA, ³Embry–Riddle Aeronautical University, Daytona Beach, FL, USA

Abstract During the “Auroral Jets” experiment from Poker Flat, Alaska on 2 March 2017, two NASA sounding rockets were simultaneously launched into the active auroral ionosphere. The rockets were equipped with instrumentation to measure DC and AC electric fields, magnetic fields, energetic electrons, plasma density, and neutral winds and achieved apogees of 190 and 330 km. A prominent feature of the electric and magnetic field observations is the presence of localized large-amplitude (± 40 mV/m and ± 100 nT) small-scale ($\lambda_{\perp} \sim 1$ km) Alfvén wave structures at altitudes as low as 150 km in the vicinity of up- and down-ward current regions. We interpret the oscillations as representing standing waves associated with the ionospheric Alfvén resonator formed between the ionosphere and the lower magnetosphere. The electric field components of the Alfvén waves show signatures of wave steepening in correlation with electron precipitation and large variations of the background plasma density. The signatures are discussed in the context of nonlinear evolution of the ionospheric feedback instability.

1. Introduction

Alfvén waves are fundamental features of magnetized plasmas and participate in various processes on different temporal and spatial scales. In the Earth’s high-latitude ionosphere, for example, they induce, via electron acceleration, a range of intriguing micro-scale plasma processes involving high-frequency waves (e.g., Akbari et al., 2012, 2020); they are thought to be responsible for the generation of fine-scale features of auroral arcs (e.g., Semeter et al., 2008); and, on larger scales, are an important component of magnetosphere-ionosphere interactions (e.g., Verkhoglyadova et al., 2018). By accelerating magnetospheric electrons (Chaston et al., 2002; Kletzing & Hu, 2001), heating ionospheric ions, and by carrying field-aligned currents and Poynting flux, Alfvén waves facilitate the exchange of mass, momentum, and energy between the ionosphere and the magnetosphere.

Some of the most compelling observations of Alfvén waves are obtained in the ionosphere and the lower magnetosphere in the form of small-scale, localized, ultra-low-frequency (ULF) electromagnetic waves near auroral arcs (e.g., Cohen et al., 2013). Such observations are often associated with the ionospheric Alfvén resonator (IAR)—a resonant cavity formed between the conductive E region of the ionosphere and a region of a strong gradient in Alfvén speed in the lower magnetosphere (Lessard & Knudsen, 2001; Lysak, 1988, 1991; Pokhotelov et al., 2000; Trakhtengerts & Fel’Dshtein, 1987). The resonator can trap Alfvén waves by partial reflection at its boundaries, forming a standing wave pattern. Under favorable conditions, the trapped waves may become unstable to the Ionospheric Feedback Instability (IFI; Atkinson, 1970; Lysak & Song, 2002; Sato, 1978; Streltsov & Lotko, 2004; Tulegenov & Streltsov, 2017) and grow to large amplitudes where they can further modify the ionosphere via the current they carry or via the Ponderomotive force of their electric fields (Streltsov & Lotko, 2008).

The ionospheric feedback instability is based on the idea that an initial field-aligned current (FAC), j_{\parallel} , modifies the E region plasma density (equivalently, conductivity) via adding or removing electrons. This modification, in the presence of the background convection electric field, produces secondary j_{\parallel} , further modifying the conductivity. This feedback mechanism is the consequence of the density and current continuity equations in the ionospheric E region: $\frac{\partial n}{\partial t} = \frac{j_{\parallel}}{eh} + \alpha(n_0^2 - n^2)$ and $\nabla \cdot (\Sigma_p \mathbf{E}_{\perp}) = -j_{\parallel}$, respectively (Lysak, 1991; Sato, 1978); where, Σ_p is the height-integrated Pedersen conductivity, \mathbf{E}_{\perp} is the perpendicular electric field in the ionosphere, n and n_0 are the plasma density and its background value, α is the recombination coefficient, and e and h are the elementary charge and the effective thickness of the ionospheric E layer. In the context of Alfvén waves, the initial field-aligned

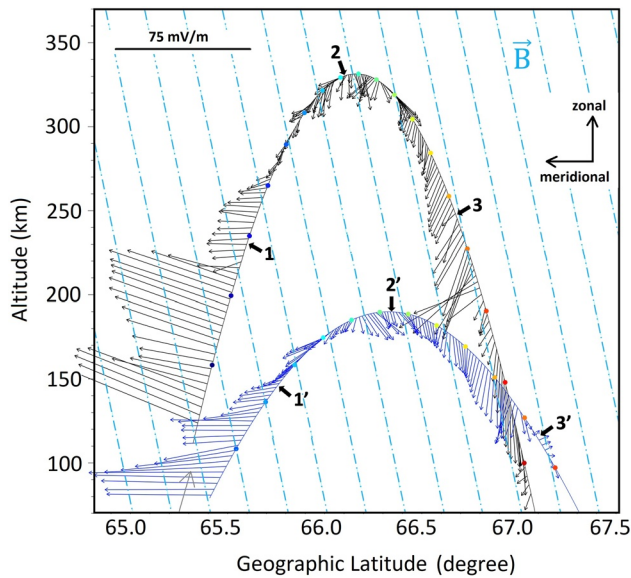


Figure 1. The trajectory of the two payloads in geographic coordinates. Superimposed on the trajectories are the perpendicular components of the DC electric field with a maximum amplitude of 75 mV/m. The background magnetic field lines are shown with dashed blue lines. The color-coded circles on the trajectories represent the location of the payloads at different times in increments of 25 s. Six intervals of wave activity (“events”) are identified with black arrows which will be further discussed.

current is that of a downgoing wave and the secondary j_{\parallel} is associated with the emission of an upward Alfvén wave from the ionosphere. The ionospheric feedback instability can then be explained in terms of “overreflection,” where the amplitude of the wave reflected from the ionosphere is larger than that of the incident wave due to the emission of the secondary current (Lysak & Song, 2002; Pokhotelov et al., 2001; Trakhtengerts & Fel’Dshtein, 1991). In addition to the overreflection, there exist other conditions for the instability to grow. Such details of the ionospheric feedback instability, including the dispersion relation of the growing modes, the instability threshold, and the growth rate are discussed by Lysak (1991) and Lysak and Song (2002). The ionospheric feedback instability and the generation of small-scale Alfvén waves in association with field-aligned currents have also been studied in many numerical works (e.g., Streltsov & Lotko, 2004, 2008). It is also known that the magnetic perturbations associated with IFI may reach to the ground and be detected via ground-based magnetometers (e.g., Beggan, 2014; Belyaev et al., 1999).

In this work, we present recent results from a sounding rocket experiment where ULF oscillations are observed in DC electric and magnetic fields at altitudes as low as 120 km. We discuss a group of waves observed near 250 km as representing standing waves associated with the ionospheric Alfvén resonator. The electric field components of the Alfvén waves include signatures of wave steepening in correlation with large variations of the background plasma density that may result from a nonlinear evolution of the ionospheric feedback instability. The results are compared to previously published numerical studies of Alfvén waves in the lower auroral ionosphere and with other sounding rocket observations.

2. Observations

The Auroral Jets dual-sounding rocket experiment was launched from Poker Flat, Alaska on 2 March 2017. The experiment was designed to investigate, among other topics, dynamics of auroral arcs by collecting simultaneous in-situ measurements on similar magnetic field lines at two altitudes. The two instrument payloads—each, equipped with electric and magnetic field sensors, energetic electron instruments, and plasma density probes—simultaneously achieved their apogees of 190 (hereafter called the “low-flyer”) and 330 km (the “high-flyer”). The sounding rocket experiment was coordinated with ground-based observations by the Poker Flat Incoherent Scatter Radar (PFISR) and optical imagers operated by the University of Alaska. A detailed description of the experiment design and instrumentation will be published elsewhere.

Figure 1 shows the trajectory of the payloads as a function of altitude and geographic latitude. The two rockets were launched in the northward direction such that their trajectories remained roughly at a constant geographic longitude of $\sim 147.5^{\circ}\text{W}$, obtaining a maximum separation of ~ 10 km in the east-west direction. Superimposed on the trajectories are the perpendicular components of the DC electric field in the magnetic zonal and meridional directions. Electric field measurements were obtained on the surface perpendicular to payloads’ spin axis, which throughout the flights were aligned in the direction of the magnetic field. Consequently, full components of the electric field were measured in directions perpendicular to the magnetic field while no information was obtained in the parallel direction. Also superimposed on the trajectories are color-coded circles that represent the location of the payloads at different times in increments of 25 s. The same colors at the peaks of the trajectories indicate that the two payloads achieved their apogees simultaneously.

The countdown for the two launches started during the growth phase of a substorm, where an arc located north of Poker Flat was expanding southward. As shown in Figure 1, during the upleg of the flights northward DC electric fields of magnitude ~ 75 mV/m were observed, consistent with data from the PFISR and the convection patterns from the Super Dual Auroral Radar Network (SuperDARN). However, before the payloads reached their apogees, the arc broke up, leading to a dynamic environment with variable auroral features and in-situ electric fields.

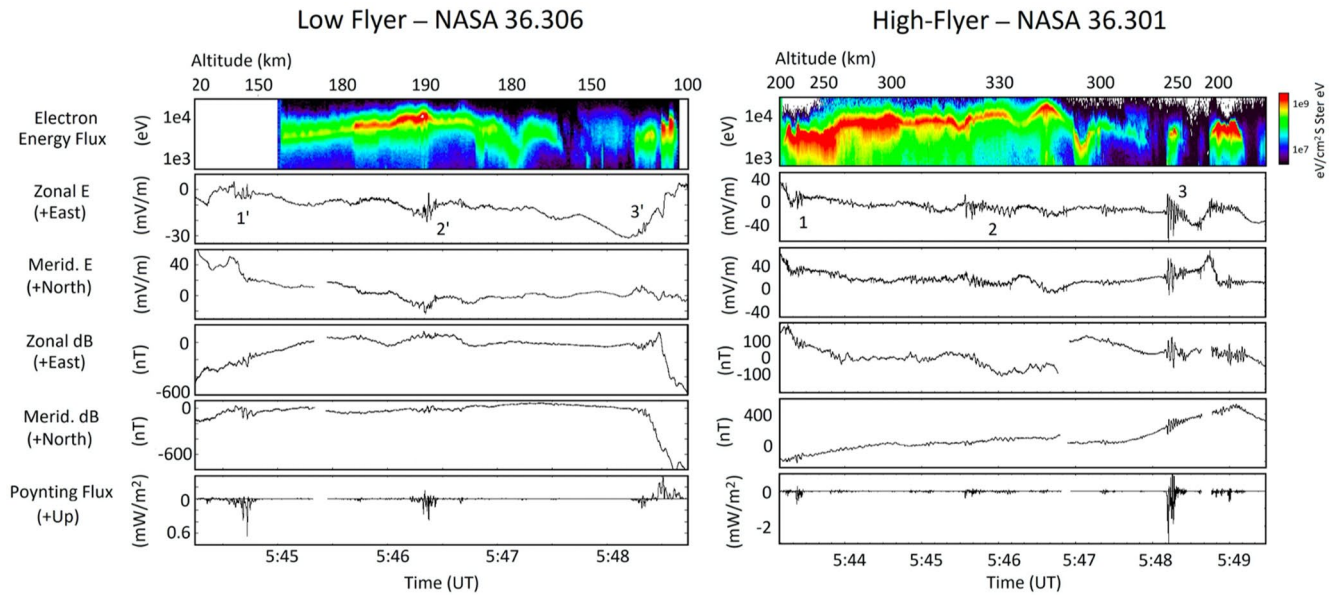


Figure 2. Summary plots of particle and field measurements from the low- and the high-flyer payloads are shown in the left and right panels, respectively. Shown, from top to bottom, are the omni-directional energetic electron flux; the zonal and the meridional components of the DC electric field; the zonal and meridional components of the magnetic field fluctuations; and the field-aligned Poynting flux. Several periods of strong wave activity (“events”) in the electric and magnetic field data are tagged in both the high- and low-flyer data. Several instances of discontinuity in the electric field, magnetic field, and Poynting flux are due to interference and have been removed to avoid unnecessary attention. The local time in Poker Flat, AK is UTC−9 hr .

Strong wave activities, extending to altitudes as low as 150 km, were observed throughout the flights in both the electric and magnetic field measurements. A summary of particles and fields data from the low-flyer rocket is shown in the left panels of Figure 2. Here, the top panel shows the omni-directional energetic electron flux. The next four panels show the zonal and the meridional components of the DC electric field and the zonal and meridional components of the magnetic field fluctuations. The latter two are obtained by subtracting the measured fields from the predictions of the IGRF model. The bottom panel shows the field-aligned Poynting flux calculated from the electric and magnetic field measurements. In the same format as those in the left panels, results from the high-flyer payload are shown on the right. Several periods of strong wave activity (“events”) in the electric and magnetic field data are tagged in the zonal component of the electric field in both the high- and low-flyer data. These correspond to the intervals marked in Figure 1 by black arrows. In order to aid the comparison between the two sets of measurements, the detrended zonal electric field and the meridional magnetic field data from the two payloads are repeated in Figure 3 as a function of magnetic latitude.

Prominent features of the observations shown in Figure 2 include two intervals of strong Alfvén wave activity in the high-flyer data, identified as events 2 and 3. Enlargements of these intervals are shown in Figure 4. We begin with a discussion of event 2 which is presented in the left panels. The Alfvén waves that constitute event 2 were observed within a broad “inverted V” type electron feature whose peak energy reached 10 keV. Electric and magnetic field oscillations with various frequencies are present, primarily carrying a downward Poynting flux. Between 5:45:55 and 5:46:15 UT, relatively monochromatic oscillations at 0.25 Hz are observed in the zonal electric field (E_{zon}) and the meridional magnetic field (B_{mer}). The ratio of $\frac{\Delta E_{zon}}{\Delta B_{mer}} \approx \frac{17 \text{ mV/m}}{35 \text{ nT}}$ is close to the Alfvén speed of 700 km/s calculated from the measured plasma density of $n_e = 1.5 \times 10^{11} \text{ m}^{-3}$, assuming $M_i = 16$. At the altitude of the observations in the lower ionosphere the electron inertial length, $\lambda_e = \frac{c}{\omega_{pe}} \sim 10 \text{ m}$, is small compared to the perpendicular wavelength, $\lambda_{\perp} \sim 2 \text{ km}$, and the modification of the Alfvén wave dispersion relation due to electron inertial effects is negligible. The ratio of $\Delta E/\Delta B$ around $V_A \sqrt{(1 + k_{\perp}^2 \lambda_e^2)} \approx V_A$, thus, identifies the observed electromagnetic fluctuation as of Alfvénic nature. In the above equations, c is the speed of light, ω_{pe} is the angular electron plasma frequency, V_A is the local Alfvén speed, and λ_{\perp} and k_{\perp} are the perpendicular wavelength and wavenumber associated with the oscillations. The latter two are obtained given the northward $\sim 500 \text{ m/s}$ velocity of the payload and the assumption that the oscillations represent spatial variations that are static during the passage of the payload. As will be discussed in the following, this assumption is not necessarily

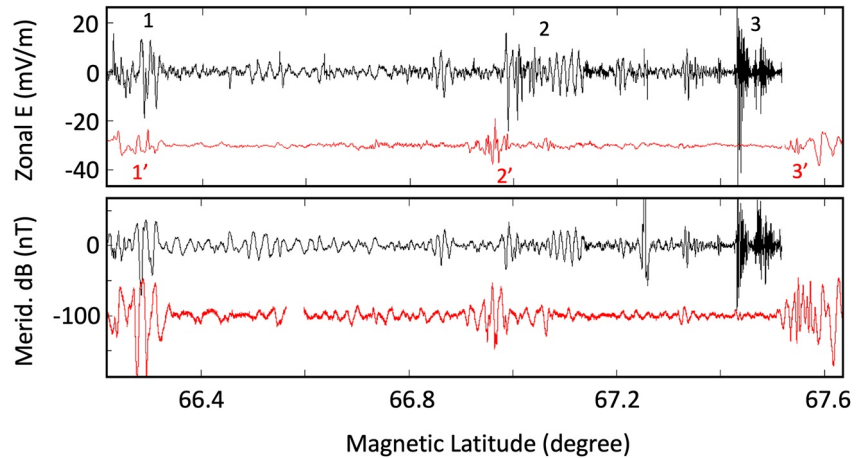


Figure 3. (Top) detrended zonal electric field and (bottom) meridional magnetic field from the high- (black) and low-flyer (red) as a function of magnetic latitude. For better representation, the red curves are shifted toward negative values by 30 mV/m and 100 nT. The three events identified in Figures 1 and 2 are tagged in the top panel.

correct since the small-scale Alfvén waves could have a phase velocity of the order of km/s in $\perp B$ directions. This, however, will not significantly affect our analysis at this time. The electric and magnetic oscillations are roughly $\pi/2$ out of phase, consistent with the interpretation of a standing wave pattern (Clemmons et al., 2000). The Poynting flux oscillates at twice the frequency of E_{zon} and B_{mer} while remaining mostly downward. The bias in the Poynting flux toward negative values indicates that a portion of the flux is likely converted to Joule heating at altitudes below the payload. A careful examination of the electron flux at this time reveals modest modulations of the peak energy of the keV electrons that appear correlated with the electric and magnetic field variations.

In the same format as the left panels, the right panels in Figure 4 show an interval in the vicinity of the event 3 in Figure 2. Here, large-amplitude oscillations are observed in both perpendicular components of the electric and magnetic fields. At around 5:48:12 UT, the amplitude of the oscillations in E_{zon} and B_{mer} reaches to values as

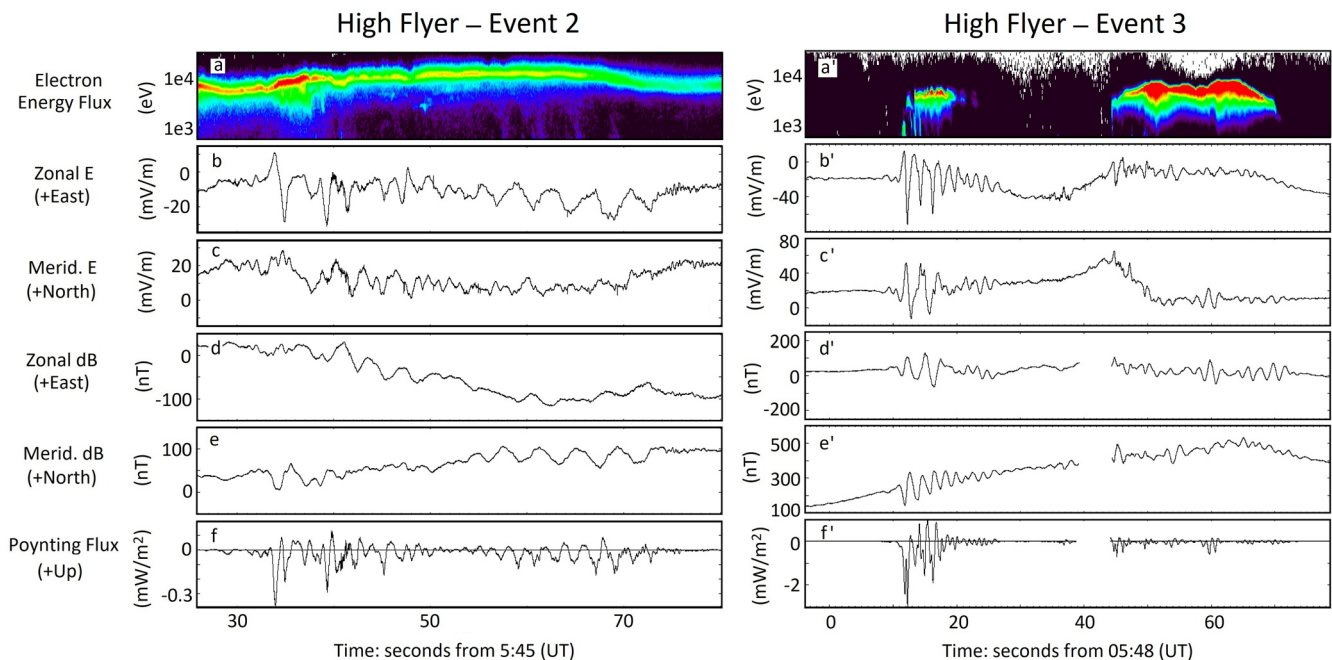


Figure 4. Enlargements of two intervals in the vicinity of event 2 (left panels) and event 3 (right panels) identified in the high-flyer data in Figure 2. Shown are the electron differential energy flux, oscillations in the electric and magnetic fields, and the Poynting flux. The format is the same as that in Figure 2.

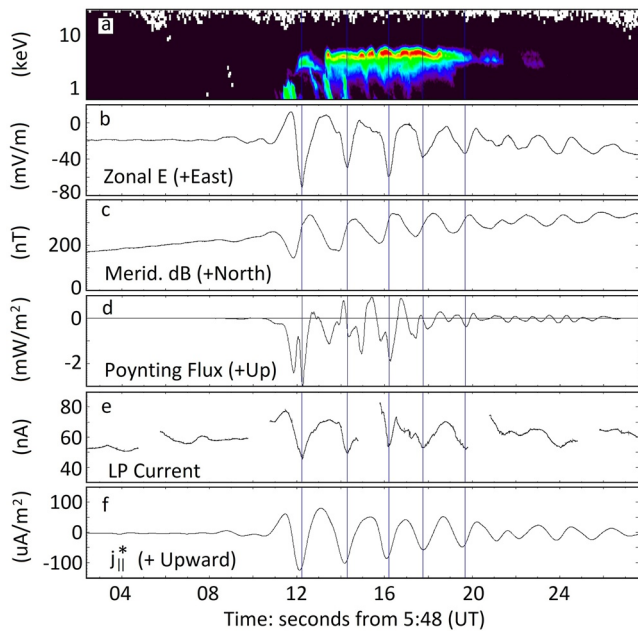


Figure 5. An enlargement illustrating the onset of Alfvén waves for event 3 shown in Figure 4. Energetic electron flux (a), the zonal component of the electric field (b), and the meridional component of the magnetic field fluctuations (c) are correlated with the Poynting flux (d), Langmuir probe's ion current (e) and the field-aligned current density (f) determined from vector magnetic field data. The gaps in Langmuir probe's data are associated with Current-Voltage (I–V) sweeps that are removed in order to direct attention to periods of fixed bias voltage. In the bottom panel, $j_{||}$ is marked with “*,” indicating that the calculated current densities are subject to large variations based on the values assumed for unknown parameters—specifically, the perpendicular phase velocity of the waves.

large as ± 40 mV/m and ± 100 nT, respectively, corresponding to the ratio of $\Delta E_{zonal}/\Delta B_{mer} = 400$ km/s. This is comparable to the Alfvén speed of 500 km/s derived from the measured electron density of $n_e = 4 \times 10^{11} \text{ m}^{-3}$, assuming $M_i = 20$ (a mixture of O^+ and molecular ions). A similar ratio is obtained for $\Delta E_{mer}/\Delta B_{zonal}$, although, E_{zonal} and E_{mer} (and similarly B_{mer} and B_{zonal}) appear to oscillate with different periods at the beginning of the event around 5:48:15 UT. A phase shift of $\sim \pi/2$ is also observed between the conjugate electric and magnetic oscillations. This, along with the oscillatory form of the Poynting flux, is interpreted as the signature of a standing wave pattern. The largest oscillations are observed at the leading edge of an isolated period of energetic electrons (panel a') that show modulations in their peak energy of ~ 5 keV. Below the peak energy, there exist signatures of electron acceleration by inertial Alfvén waves—presumably accelerated at much higher altitudes where inertial effects are important. These appear in the form of bands extending from 1 to 3 keV down to 600 eV, the lowest energy range measured by the instrument. Electron flux accelerated by inertial Alfvén waves typically extend to energies as low as 100 eV. At later times, between 4:48:40–5:49:10 UT, energetic inverted V electrons are again observed which coincide with a sudden increase in the background electron temperature measured by Langmuir probes (data not shown). Electromagnetic oscillations extend to this interval, although with much smaller amplitudes.

Returning to the top panel of Figure 3, it is clear that several important features in the electric field measurements observed by the high-flyer are not present in low-flyer data. Specifically, the large-amplitude quasi-coherent oscillations identified as standing waves (i.e., events 2 and 3 in Figure 2) are not observed by the low-flyer. Instead, electric field fluctuations with significantly smaller amplitudes are observed. This is despite the fact that at the time of the events the two payloads were probing similar magnetic field lines at around the same times (compare the color-coded circles superimposed on the trajectories in Figure 1). It is possible that the waves are attenuated by the finite ionospheric conductivity before reaching the lower payload (Lysak et al., 2013). Looking at the meridional magnetic fields in the bottom panel

of Figure 3, however, we find that magnetic field oscillations with similar amplitudes and frequencies as those observed by the high-flyer are present in the low-flyer data. It is, therefore, possible that the absence of the quasi-coherent electric field oscillations in the low-flyer measurements is a consequence of the standing wave pattern, for which the boundary conditions in the E region enforce a null in perpendicular electric fields (thus, a rapid decrease in amplitude as a function of altitude) and a maximum in the magnetic fields.

An interesting aspect of the observations presented in Figure 4 are the signatures of wave steepening in the zonal component of the electric field (panel b') which is accompanied by an overall asymmetry of the oscillations toward negative values. This feature is further explored in Figure 5 where the electric and magnetic field data are shown along with the ion current obtained by a cylindrical Langmuir probe operating at a fixed bias of $V_b = -3$ V, and the field-aligned current density $j_{||}$ derived from the curl of the vector magnetic field measurements. Also shown in Figure 5 are the energetic electron flux and the Poynting flux. Langmuir probe's ion current (shown in Figure 5e) is proportional to the local plasma density. Its variations are, therefore, interpreted as significant modulations of the background plasma density that are clearly correlated with the steepened features in the zonal electric field. At the time of these measurements, the Langmuir probe is located in the ram direction of the payload and is not affected by the plasma wake produced by the moving body. The gaps in the Langmuir probe's current are associated with intervals of Current-Voltage (I–V) sweep that are regularly performed to determine the electron temperature and the payload's potential. These intervals are removed in order to direct the attention to the periods of fixed bias voltage.

In the bottom panel of Figure 5, the derivation of the field-aligned current density from the magnetic field data via the relation $\mathbf{j} = 1/\mu_0 \nabla \times \mathbf{B}$ is based on several assumptions which need clarification. First, as mentioned

before, we note in Figures 4b'–4e' that dB_{mer} and E_{zon} appear to be oscillating at a different frequency than dB_{zon} and E_{mer} —possibly indicating the presence of separate waves whose electric and magnetic fields only appear in either the zonal or the meridional direction. In this case, the oscillations in dB_{mer} and E_{zon} may be identified as a wave with a north-south-directed phase front, propagating in the zonal direction. This can be considered in the context of the observed northward dB between 5:48:00–5:48:50 UT—consistent with a latitudinal upward current sheet—and a south-westward plasma flow of ~ 800 m/s. Given the northward trajectory of the payload the static current sheet approximation to calculated field-aligned current densities from magnetic field data may not be accurate. Instead, we calculate j_{\parallel} by assuming that the oscillations are associated with waves with a predominantly westward wave vector in $\perp B$ directions with the phase velocity of 2 km/s. The calculations are extremely sensitive to the assumed parameters; accordingly, in Figure 5f, j_{\parallel} is marked with “*,” indicating that the calculated currents are subject to large variations based on the values assumed for the unknown parameters.

3. Discussion

In the previous section, the large-amplitude oscillations in the electric and magnetic fields are interpreted in terms of standing wave patterns, potentially associated with Alfvén waves trapped in the ionospheric Alfvén resonator. The interpretation is based on the oscillatory characteristic of the Poynting flux, the phase shift between the electric and the magnetic oscillations, and the ratio of $\Delta E/\Delta B$ in the vicinity of the local Alfvén speed. The frequencies of the oscillations, 0.25 and 0.5 Hz for events 2 and 3, fall within the range of the eigenfrequencies of the resonator between 0.1 and 1 Hz (Hiraki & Watanabe, 2011; Lysak, 1991; Trakhtengerts & Fel'Dshtein, 1987). The local time of the observations ($\sim 20:45$) is consistent with the time periods when ground-based magnetometers often show signatures of ionospheric Alfvén resonances (e.g., Beggan, 2014). Despite such clues that suggest a connection between the observations and IAR and IFI, however, there exist other observational and theoretical factors that need to be discussed. For example, amplification of trapped ULF waves by the ionospheric feedback instability should occur under favorable conditions in the ionosphere. The conditions, that are extensively discussed in the literature (e.g., Doe et al., 1995; Streltsov & Lotko, 2004), include low ionospheric conductivity and large perpendicular electric fields. Such conditions often exist in the return current regions in the vicinity of auroral arcs where conductivity is reduced by the upward motion of electrons that carry field-aligned current from the ionosphere. We note, however, that in Figure 2, both events 2 and 3 are observed in conjunction with energetic electron precipitation. Furthermore, the amplitude of the perpendicular electric field, E_{\perp} , at these times is rather modest, of the order of 30 mV/m or less.

The requirement for overreflection of Alfvén waves from the ionosphere, which is a necessary condition for the development of the feedback instability, is given by the linear theory as $\omega < k_{\perp} \cdot (\mathbf{u}_E + \gamma \mathbf{u}_d)$ (Lysak & Song, 2002). Here, \mathbf{u}_E is the $E \times B$ drift, $\mathbf{u}_d = M_P \mathbf{E}_{\perp} - M_H \mathbf{E}_{\perp} \times \hat{\mathbf{b}}$ is the relative drift between electrons and ions in the ionosphere; ω and k_{\perp} are the angular frequency and the perpendicular component of the wave vector; M_P and M_H are the Pedersen and Hall conductivity of the E region; and $\gamma = 1$, indicating that field-aligned currents are carried by thermal electrons. In situations where the upward current region is accompanied by energetic electron precipitation, γ is greater than one and accounts for the amount of extra ionization produced by the precipitating electrons. Verifying the instability requirement in our observations is difficult considering the number of unknown variables; nevertheless by assuming $\omega/2\pi = 0.5$ Hz (for event 3), $M_P = 10^4$ m²/sV, and further considering $k_{\perp} \parallel \mathbf{E}_{\perp}$, and thus ignoring the Hall conductivity, the instability threshold for $E_{\perp} \sim 30$ mV/m requires $\lambda_{\perp} < 600$ m. This implies $v_{\phi\perp} < \gamma \times 300$ m/s, where $v_{\phi\perp} = \omega/k_{\perp}$ is the perpendicular phase velocity. Assuming $\gamma = 1$ leads to $v_{\phi\perp} < 300$ m/s, which is far below the 2 km/s that was assumed in order to obtain a realistic j_{\parallel} is Figure 5f. However, the electromagnetic oscillations of event 3 are observed in the vicinity of energetic electrons for which $\gamma > 1$. Following $\gamma = 1 + e\Phi_{\parallel}/E_0$ (Lysak & Song, 2002), where $e\Phi_{\parallel} = 4.5$ keV is the characteristic energy of the precipitating electrons at the time of event 3, and $E_0 = 35$ eV is the energy required for the production of a new electron-ion pair (Rees, 1963), we have $\gamma \sim 130$, and thus the instability threshold is met as long as $v_{\phi\perp} < 40$ km/s. The above calculation of the instability threshold is clearly dependent on the accuracy of a number of assumptions that are adopted.

Another important parameter associated with the ionospheric feedback instability is the ratio of the height-integrated ionospheric Pedersen conductivity, Σ_p , and the “Alfvén conductivity” defined as $\Sigma_A = 1/\mu_0 V_A$. As discussed in many theoretical and numerical works, the “impedance matching condition”, $\Sigma_A \approx \Sigma_p$, allows Alfvén waves that are excited in the E region to efficiently couple into the resonator—an effect that maximizes the growth

rate of the instability (Lysak, 1991; Lysak & Song, 2002; Pokhotelov et al., 2001; Streltsov & Lotko, 2004). Assuming an average E region electron density of $\sim 2 \times 10^{11} \text{ m}^{-3}$, E layer thickness of $h = 20 \text{ km}$, and the ion Pedersen mobility of $M_p = 10^4 \text{ m}^2/\text{sV}$, Σ_p and Σ_A are estimated around 6.4 and 1.8 mho, respectively. Despite the fact that the impedances are not matched, the ionospheric feedback instability can still develop successfully with a smaller growth rate. In fact, $\Sigma_p > \Sigma_A$ may be a favorable condition under which a large-scale FAC splits into kilometer-scale filaments (Trakhtengerts & Fel'Dshtein, 1984).

It is helpful to consider our events in the context of the statistical study of kilometer-scale magnetic perturbations observed by the CHAMP satellite (Rother et al., 2007). Rother et al. (2007) finds that during periods of moderate geomagnetic disturbances similar to the conditions of our experiment, for which $K_p = 4.3$, magnetic field perturbations consistent with signatures of waves trapped inside the ionospheric Alfvén resonator are preferentially observed at magnetic latitudes of around $\sim 65 - 72^\circ$ —as is the case in Figure 3. They also find that the occurrence rate of the magnetic field perturbations maximizes around MLT = 12 hr, and minimizes around MLT = 18 hr; and that in the afternoon section the magnetic perturbations predominantly collocate with large-scale Region 1 upward field-aligned currents. In comparison, the magnetic perturbation events shown in Figure 2 are detected at MLT 18.5 hr, and are seen at and slightly pole-ward of a region characterized by an intense flux of precipitating electron, which statistically map to the Region 1 upward FAC (Xiong et al., 2020).

In Figure 5, the steepening of the zonal component of the electric field and the overall asymmetry toward negative (westward) values show a strong resemblance to the numerical results of Lysak and Song (2002). Similar results are also observed in the simulations of Streltsov (2018) where the signatures are discussed in terms of the nonlinear stage of the feedback instability—although, the latter work involves the global resonator formed between the conjugate ionospheres in the northern and southern hemispheres. It is expected that in the linear regime of the instability, when the amplitude of the wave's electric field and the perturbations of the ionospheric conductivity are small compared to the background quantities, the instability produces periodic fluctuations in the ionospheric conductivity, electric field, and the field-aligned current density with peaks and valleys of equal amplitudes and length scales. As the instability develops into the nonlinear regime, however, the symmetry may break; the amplitudes of the downward currents increase, and their perpendicular sizes decrease compared with those of the upward currents. The asymmetry arises as a consequence of large variations in ionospheric conductivity. Specifically, in regions of reduced conductivity, that is, in downward current regions, the electric field intensity increases in order to ensure the current closure in the ionosphere. This is accompanied by an increase in the amplitude of the downward currents and, consequently, a decrease in their width.

The observations shown in Figure 5 can be compared to the above description in several aspects. First, the large variations of the electric field and the implied plasma density compared to the background values may indicate that the instability is in the nonlinear regime. Second, the spiky peaks of the electric field coincide with the regions of plasma density depletions. This is similar to the numerical results of Lysak and Song (2002), but in contrast to the simulation results presented in Figure 3 of Streltsov (2018). While in the steady-state the downward j_{\parallel} (corresponding to upward motion of ionospheric electrons) is expected to peak at the location of the maximum density gradient, this is not necessarily the case in a dynamic situation. In fact, the phase difference between the two determines whether the perturbations decay or grow (Miura & Sato, 1980). The level of implied density variations also requires some attention. Downward field-aligned currents associated with ULF shear Alfvén waves are predominantly carried by the upward motion of ionospheric thermal electrons (Streltsov & Mishin, 2018). Assuming $\partial n_e / \partial t \approx j_{\parallel} / eh$, where h is now the effective thickness of the F region, and considering the average F region background density of $n_e \sim 2 \times 10^{11} \text{ m}^{-3}$ at the time of event 3, the $\sim 25\%$ variations in plasma density suggested in Figure 5e, over a half-wave period of 1 s and a vertical extent of $h = 150 \text{ km}$, would require a field-aligned current density of the order of 1 mA/m^2 . Such large currents, while not very common, are also implied from the magnetic field perturbations observed by the CHAMP satellite in the same magnetic latitudes and local times as our observations (Rother et al., 2007). Our estimate of the current density will decrease if we assume a lower frequency for the Alfvén waves or the background ionospheric density. Alternatively, the density variations could be associated with modulations in precipitating electron flux and the resulting ionization. Although modulations in electron flux are seen in Figure 5a, they do not appear to be correlated with the variations of Langmuir Probe's ion current shown in Panel e.

The observations presented above clearly reflect a dynamic nature of the auroral ionosphere during active periods which is difficult to fully reconstruct in numerical works. For example, the results presented here and those

reported by Cohen et al. (2013) show complex patterns of energetic electron flux in conjunction with ULF electromagnetic oscillations. The possibility of electron acceleration by Alfvén waves trapped inside the ionospheric Alfvén resonator or by Alfvén waves propagating along plasma density cavities is studied by several works (e.g., Chaston et al., 2002; Mottez & Génot, 2011; Trakhtengerts & Fel’Dshtein, 1991). While we cannot explain all the observational features at this time, the observations should be helpful in guiding future simulations.

4. Summary

An unprecedented set of observations of particles and fields in the auroral ionosphere obtained by a dual-sounding rocket experiment is presented. Localized, large-amplitude (± 40 mV/m and ± 100 nT), small-scale ($\lambda_{\perp} \sim 1$ km) Alfvén wave structures are observed at altitudes as low as 150 km in the vicinity of up- and downward current regions. The oscillations are interpreted as standing waves trapped inside the ionospheric Alfvén resonator that are likely amplified by the ionospheric feedback instability. The electric field components of the Alfvén waves show signatures of wave steepening in correlation with electron precipitation and large ($\sim 25\%$) variations of the background plasma density. Aspects of the observations strikingly resemble numerical results that are interpreted as the nonlinear regime of the ionospheric feedback instability.

Data Availability Statement

The data used to conduct this research can be accessed at <https://doi.org/10.5281/zenodo.5889351>.

Acknowledgments

Hassanali Akbari is a Fellow of the NASA Postdoctoral Program.

References

- Akbari, H., Labelle, J. W., & Newman, D. L. (2020). Langmuir turbulence in the auroral ionosphere: Origins and effects. *Frontiers in Astronomy and Space Sciences*, 7, 116. <https://doi.org/10.3389/fspas.2020.617792>
- Akbari, H., Semeter, J., Dahlgren, H., Diaz, M., Zettergren, M., Strømme, A., & Heinselman, C. (2012). Anomalous ISR echoes preceding auroral breakup: Evidence for strong Langmuir turbulence. *Geophysical Research Letters*, 39(3), 3102. <https://doi.org/10.1029/2011GL050288>
- Atkinson, G. (1970). Auroral arcs: Result of the interaction of a dynamic magnetosphere with the ionosphere. *Journal of Geophysical Research*, 75(25), 4746–4755. <https://doi.org/10.1029/ja075i025p04746>
- Beggan, C. D. (2014). Automatic detection of ionospheric Alfvén resonances using signal and image processing techniques. *Annales Geophysicae*, 32, 951–958. <https://doi.org/10.5194/angeo-32-951-2014>
- Belyaev, P. P., Bösinger, T., Isaev, S., & Kangas, J. (1999). First evidence at high latitudes for the ionospheric Alfvén resonator. *Journal of Geophysical Research*, 104(A3), 4305–4317. <https://doi.org/10.1029/1998ja900062>
- Chaston, C., Bonnell, J., Carlson, C., Berthomier, M., Peticolas, L., Roth, I., & Strangeway, R. (2002). Electron acceleration in the ionospheric Alfvén resonator. *Journal of Geophysical Research*, 107(A11). SMP–41. <https://doi.org/10.1029/2002JA009272>
- Clemmons, J., Pfaff, R., Lennartsson, O., Mozer, F., Singer, H., Peterson, W., et al. (2000). Observations of traveling Pc5 waves and their relation to the magnetic cloud event of January 1997. *Journal of Geophysical Research*, 105(A3), 5441–5452. <https://doi.org/10.1029/1999ja900418>
- Cohen, I., Lessard, M., Kaeppler, S., Bounds, S., Kletzing, C., Streltsov, A., et al. (2013). Auroral Current and Electrodynamics Structure (ACES) observations of ionospheric feedback in the Alfvén resonator and model responses. *Journal of Geophysical Research: Space Physics*, 118(6), 3288–3296. <https://doi.org/10.1002/jgra.50348>
- Doe, R., Vickrey, J., & Mendillo, M. (1995). Electrodynamic model for the formation of auroral ionospheric cavities. *Journal of Geophysical Research*, 100(A6), 9683–9696. <https://doi.org/10.1029/95ja00001>
- Hiraki, Y., & Watanabe, T. (2011). Feedback instability analysis for dipole configuration with ionospheric and magnetospheric cavities. *Journal of Geophysical Research* 116(A11). <https://doi.org/10.1029/2011ja016721>
- Kletzing, C., & Hu, S. (2001). Alfvén wave generated electron time dispersion. *Geophysical Research Letters*, 28(4), 693–696. <https://doi.org/10.1029/2000gl012179>
- Lessard, M., & Knudsen, D. (2001). Ionospheric reflection of small-scale Alfvén waves. *Geophysical Research Letters*, 28(18), 3573–3576. <https://doi.org/10.1029/2000gl012529>
- Lysak, R. L. (1988). Theory of auroral zone PiB pulsation spectra. *Journal of Geophysical Research*, 93(A6), 5942–5946. <https://doi.org/10.1029/ja093ia06p05942>
- Lysak, R. L. (1991). Feedback instability of the ionospheric resonant cavity. *Journal of Geophysical Research*, 96(A2), 1553–1568. <https://doi.org/10.1029/90ja02154>
- Lysak, R. L., & Song, Y. (2002). Energetics of the ionospheric feedback interaction. *Journal of Geophysical Research*, 107(A8). SIA 6-1–SIA 6-13. <https://doi.org/10.1029/2001ja000308>
- Lysak, R. L., Waters, C. L., & Sciffer, M. D. (2013). Modeling of the ionospheric Alfvén resonator in dipolar geometry. *Journal of Geophysical Research: Space Physics*, 118(4), 1514–1528. <https://doi.org/10.1002/jgra.50090>
- Miura, A., & Sato, T. (1980). Numerical simulation of global formation of auroral arcs. *Journal of Geophysical Research*, 85(A1), 73–91. <https://doi.org/10.1029/ja085ia01p00073>
- Mottez, F., & Génot, V. (2011). Electron acceleration by an Alfvénic pulse propagating in an auroral plasma cavity. *Journal of Geophysical Research*, 116(9). <https://doi.org/10.1029/2010JA016367>
- Pokhotelov, O. A., Khrushev, V., Parrot, M., Senchenkov, S., & Pavlenko, V. (2001). Ionospheric Alfvén resonator revisited: Feedback instability. *Journal of Geophysical Research*, 106(A11), 25813–25824. <https://doi.org/10.1029/2000ja000450>
- Pokhotelov, O. A., Pokhotelov, D., Streltsov, A., Khrushev, V., & Parrot, M. (2000). Dispersive ionospheric Alfvén resonator. *Journal of Geophysical Research*, 105(A4), 7737–7746. <https://doi.org/10.1029/1999ja900480>

- Rees, M. H. (1963). Auroral ionization and excitation by incident energetic electrons. *Planetary and Space Science*, *11*(10), 1209–1218. [https://doi.org/10.1016/0032-0633\(63\)90252-6](https://doi.org/10.1016/0032-0633(63)90252-6)
- Rother, M., Schlegel, K., & Lühr, H. (2007). CHAMP observation of intense kilometer-scale field-aligned currents, evidence for an ionospheric Alfvén resonator. *Annales Geophysicae*, *25*, 1603–1615. <https://doi.org/10.5194/angeo-25-1603-2007>
- Sato, T. (1978). A theory of quiet auroral arcs. *Journal of Geophysical Research*, *83*(A3), 1042–1048. <https://doi.org/10.1029/ja083ia03p01042>
- Semeter, J., Zettergren, M., Diaz, M., & Mende, S. (2008). Wave dispersion and the discrete aurora: New constraints derived from high-speed imagery. *Journal of Geophysical Research* *113*(A12). <https://doi.org/10.1029/2008ja013122>
- Streltsov, A. (2018). On the asymmetry between upward and downward field-aligned currents interacting with the ionosphere. *Journal of Geophysical Research: Space Physics*, *123*(11), 9275–9285. <https://doi.org/10.1029/2018ja025826>
- Streltsov, A., & Lotko, W. (2004). Multiscale electrodynamics of the ionosphere-magnetosphere system. *Journal of Geophysical Research* *109*(A9). <https://doi.org/10.1029/2004ja010457>
- Streltsov, A., & Lotko, W. (2008). Coupling between density structures, electromagnetic waves and ionospheric feedback in the auroral zone. *Journal of Geophysical Research* *113*(A5). <https://doi.org/10.1029/2007ja012594>
- Streltsov, A., & Mishin, E. V. (2018). On the existence of ionospheric feedback instability in the Earth's magnetosphere-ionosphere system. *Journal of Geophysical Research: Space Physics*, *123*(11), 8951–8957. <https://doi.org/10.1029/2018ja025942>
- Trakhtengerts, V. Y., & Fel'Dshtein, A. Y. (1984). Quiet auroral arcs: Ionosphere effect of magnetospheric convection stratification. *Planetary and Space Science*, *32*(2), 127–134.
- Trakhtengerts, V. Y., & Fel'Dshtein, A. Y. (1987). Turbulent regime of magnetospheric convection. *Geomagnetizm i Aeronomiia*, *27*, 258–264.
- Trakhtengerts, V. Y., & Fel'Dshtein, A. Y. (1991). Turbulent Alfvén boundary layer in the polar ionosphere: 1. Excitation conditions and energetics. *Journal of Geophysical Research*, *96*(A11), 19363–19374. <https://doi.org/10.1029/91ja00376>
- Tulegenov, B., & Streltsov, A. (2017). Ionospheric Alfvén resonator and aurora: Modeling of MICA observations. *Journal of Geophysical Research: Space Physics*, *122*(7), 7530–7540. <https://doi.org/10.1002/2017ja024181>
- Verkhoglyadova, O. P., Meng, X., Mannucci, A. J., & McGranaghan, R. M. (2018). Semianalytical estimation of energy deposition in the ionosphere by monochromatic Alfvén waves. *Journal of Geophysical Research: Space Physics*, *123*(6), 5210–5222. <https://doi.org/10.1029/2017ja025097>
- Xiong, C., Stolle, C., Alken, P., & Rauberg, J. (2020). Relationship between large-scale ionospheric field-aligned currents and electron/ion precipitations: DMSP observations. *Earth Planets and Space*, *72*(1), 1–22. <https://doi.org/10.1186/s40623-020-01286-z>